Semiclassical molecular dynamics simulations of intramolecular proton transfer in photoexcited 2-(2′-hydroxyphenyl)–oxazole

Victor Guallar, Victor S. Batista, and William H. Miller
Department of Chemistry, University of California, and Chemical Sciences Division, Lawrence Berkeley National Laboratory, Berkeley, California 94720

(Received 11 July 2000; accepted 8 September 2000)

A full-dimensional excited state potential energy surface is constructed, and the proton transfer dynamics associated with the keto-enolic tautomerization reaction in photoexcited 2-(2′-hydroxyphenyl)–oxazole is simulated according to an approximate version of the semiclassical initial value representation method introduced by Miller and co-workers [V. Guallar, V. S. Batista, and W. H. Miller, J. Chem. Phys. **110**, 9922 (1999)]. The full-dimensional potential energy surface is developed according to an *ab initio* reaction surface model obtained at the CIS level of quantum chemistry. Proton transfer is found to be substantially affected by isotopic substitution, and significantly coupled to the internal oxazole–hydroxyphenyl in-the-plane bending mode. The nascent tautomer is found to be stabilized primarily through vibrational energy redistribution into all of the remaining in-the-plane vibrational modes. The accuracy of the methodology is verified by reducing the dimensionality of the system and comparing our semiclassical results with full quantum mechanical calculations. © *2000 American Institute of Physics.* [S0021-9606(00)01845-6]

I. INTRODUCTION

Excited state intramolecular proton transfer (ESIPT) reactions have been extensively investigated[1–13] because of their importance in biological systems,[14–17] as well as in technological applications that include photostabilizers,[18–21] UV filter materials,[22] and information storage devices.[23–25] In general, however, the ultrafast dynamics mechanisms involved in ESIPT reactions are yet to be fully understood, and constitute a subject of much current experimental interest.[26–31] Recent experiments involve state-of-the-art femtosecond time-resolved spectroscopy where the signals are the result of complicated nuclear dynamics, the details of which cannot be extracted by a cursory examination of the results. Therefore, it is essential to combine experimental studies with theoretical simulations that face the challenge of yielding a comprehensive understanding of the underlying ultrafast reaction dynamics. In this paper we present the first molecular dynamics simulation study of the ESIPT dynamics associated with the keto–enolic tautomerization reaction of photoexcited 2-(2′-hydroxyphenyl)–oxazole (HPO), described by the structural diagram of Fig. 1.

Experimental studies of ESIPT reactions involve the observation and analysis of dual bands in the fluorescence spectra, with large Stokes-shifts suggesting the presence of both tautomeric forms. Although experimental studies of ESIPT are yet to be carried out in HPO, several systems similar to the HPO molecule have been the subject of experimental studies, including hydroxyphenyl derivatives of benzoxazole,[5–7] benzimidazol,[9,10] benzothiazole,[6,8] and more recently 2-(2′-hydroxyphenyl)-5-phenyloxazole (HPPO).[32] The 2-(2′-hydroxyphenyl)-4-methyloxazole molecule (HPMO) is the most similar system to HPO that has been studied experimentally, and its spectroscopy is expected to be very similar to the spectroscopy of HPO, since the only structural difference between the two molecules is the methyl substitutional group in the oxazole residue. Figure 2 shows the experimental HPMO absorption spectrum, with a large Stokes-shifted fluorescence band,[33] and a biexponential femtosecond fluorescence transient decay signal that has been assigned in terms of the time-dependent reactant (enol) population decay.[34] The interpretation of the experimental data presented in Fig. 2 was based on the coupling between the ultrafast proton motion, and a slower picosecond out-of-the-plane rotational motion around the C–C bond that links the hydroxyphenyl with the 4-methyloxazole functional group (see C_1-C_2 bond in Fig. 1).[34,35] The semiclassical results reported in this paper, however, suggest an ESIPT mechanism where proton motion is significantly coupled to in-the-plane vibrational modes, but approximately uncoupled from out-of-the-plane rotations. Furthermore, semiclassical calculations predict the HPO absorption spectrum to be a broad band with a very diffused superimposed vibrational structure.

In recent years, there has been a significant progress in the development of computational methods able to provide accurate descriptions of proton transfer reactions.[36–51] However, applications to ESIPT reactions of realistic systems have been hindered by the difficulty of modeling multiple time scale dynamics in electronic excited states, where proton tunneling coupled to the motion of the other degrees of freedom in the system can be significant at low temperature and determine the rate of the overall chemical reaction. The only application of semiclassical molecular dynamics to investigate a real excited state proton transfer reaction to date, has been our study of double proton transfer dynamics in a DNA base-pair model.[52] These simulations, therefore, con-

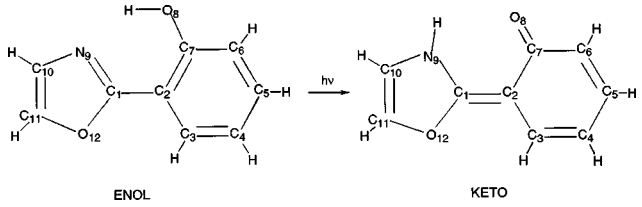

FIG. 1. Molecular structural diagram describing the ESIPT reaction in photoexcited 2-(2′-hydroxyphenyl)–oxazole (HPO).

stitute the first attempt to give a rigorous interpretation of ESIPT experiments in terms of a quantitative description of excited state proton transfer from first principles.

In an effort to investigate the excited state potential energy surface (PES) that describes the proton transfer associated with the HPO tautomerization reaction, the fully optimized geometries of the three stationary points in the $S1$ electronic excited state have been computed at the *ab initio* CIS level of quantum chemistry.[33] The proton transfer rate constant could be estimated in terms of the instanton expression,[40] simply by assuming an energy interpolating curve between the three stationary points. Such an approach has been implemented for studying various other proton transfer reactions,[53,54] but might not necessarily yield a proton tunneling rate constant for the HPO system that bears any simple relation to the true rate constant at low temperatures. The reason for this is that such an approximation assumes a reaction path through stationary points that might not necessarily correspond to the true sequence of configurations made energetically accessible to the system by the mechanism of internal energy redistribution. It is thus necessary to carry out more realistic calculations that do not assume the system to be confined to small amplitude fluctuations around any reaction path. This can be accomplished, as presented in this paper, by first calculating the full *ab initio* Born–Oppenheimer potential energy surface and then solving accurately the dynamical equations for motion on this calculated surface.

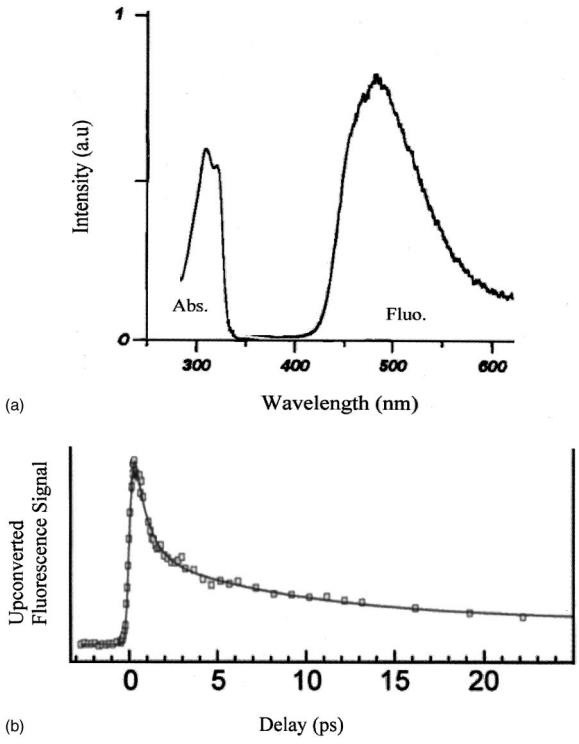

FIG. 2. (a) Experimental absorption and fluorescence spectra of 2-(2′-hydroxyphenyl)-4-methyloxazole (HPMO) in *n*-hexane at room temperature, adapted from Ref. 33. (b) Femtosecond fluorescent transient at 420 nm for HPMO in 3-methylpentane, adapted from Ref. 35. The vertical scale has been expanded by a factor of 5 beyond 350 nm.

The full-dimensional PES is developed according to the approach introduced in our previous work, as a quadratic expansion around a reaction surface potential obtained at the CIS level of quantum chemistry.[52] Such a method aims to make the best use of a reasonable number of *ab initio* calculations to map out the most relevant parts of the full-dimensional PES for the purpose of simulating reaction dynamics. The reaction surface is defined in terms of reaction coordinates chosen to be the proton displacement r_1, and the internal oxazole–hydroxyphenyl in-the-plane bending mode r_2 (see the bending angle $C_1C_2C_7$ in Fig. 1). This choice of reaction coordinates is based on the analysis of the transition state minimum energy geometry, that is planar like the keto and enol tautomeric forms, but significantly displaced along the r_1 and r_2 coordinates, relative to the keto and enol minimum energy geometries.[33] The r_2 coordinate is also expected to be strongly coupled to r_1, and promote proton transfer, since a displacement along r_2 reduces the N–O distance between the proton donor (hydroxyphenyl) and proton acceptor (oxazole) functional groups (see N_9-O_8 distance in Fig. 1), as originally observed by Ernsting and co-workers in their study of intramolecular proton transfer in 2-(2′-hydroxyphenyl)benzoxazole (HBO).[5] The reaction surface potential is obtained at various different r_2 configurations, by minimizing the $S1$ excited state potential energy of the system with respect to all other degrees of freedom $\mathbf{z}$ at the three r_2-constrained stationary points along the r_1 coordinate—i.e., enol–tautomeric form, transition state and keto–tautomeric form. The global PES is then obtained by expanding the $\mathbf{z}$ dependence to second order about the equilibrium coordinates $\mathbf{z}_0(r_1,r_2)$, using analytic CIS frequencies $\omega_0(r_1,r_2)$.

In our previous work, we limited our study to reaction dynamics simulations on a simplified three-dimensional PES, obtained by describing the motion of the locally harmonic degrees of freedom in terms of a single global variable $|\mathbf{z}|$.[52] Such a model was able to describe the early time relaxation dynamics in good qualitative agreement with recent ultrafast time-resolved spectroscopic studies,[29] but was limited with regards to modeling vibrational energy redistribution. In this paper, we treat all the vibrational degrees of freedom explicitly and we are thus able to provide a proper description of the vibrational energy redistribution. According to the results of our simulation, this complete treatment is crucial for a proper description of dynamics at long times, since the stabilization of the product tautomer involves primarily vibrational energy redistribution into most of the other in-the-plane vibrational modes.

Simulating the excited state proton transfer dynamics is particularly challenging because the protons being trans-

ferred give rise to significant quantum mechanical effects—i.e., tunneling—which cannot be described by classical molecular dynamics simulations. A number of mixed quantum-classical molecular dynamics methods have been applied to simulations of proton transfer reactions.[55–66,47] Most of these methods, however, describe the coupling between light and heavy particle degrees of freedom only approximately according to branching processes defined by stochastic hops that collapse transferring protons into either of the possible states of distinct character. Other methods are applicable only to single proton transfer reactions, or model light and heavy degrees of freedom on different ''dynamical footings''—i.e., these methods require one to specify *a priori* the ''quantum'' or ''classical'' nature of each degree of freedom in the system, and integrate their equations of motion only approximately according to a self-consistent propagation scheme.

In this paper we implement the semiclassical method introduced in our previous paper,[52] and we propagate *all* degrees of freedom on the same dynamical footing according to the classical equations of motion. We exploit the benefit of having a dynamically consistent methodology where there is no need to specify the ''quantum'' or ''classical'' nature of the degrees of freedom in the system, even in the presence of tunneling or interference effects, and we simulate proton transfer dynamics in HPO where the proton motion becomes significantly coupled to both low and high frequency reorganization coordinates. The semiclassical methodology implemented in this paper is specifically designed to avoid the computational bottleneck for applications of the SC–IVR to large molecular systems, which is caused by the calculation of the monodromy matrix elements involved in the pre-exponential factor of the semiclassical amplitude. This method reduces the computational effort necessary to integrate the N^2 coupled differential equations (where N is the number of degrees of freedom) to the integration of only N independent equations, thus scaling with molecular size in the same way as the classical trajectory equations themselves.

In our previous paper, we tested the capabilities of the approximate SC–IVR method for modeling ultrafast proton transfer by comparing our simulation results for a three-dimensional PES with full quantum mechanical calculations. The method was found to describe properly the time dependent probability of proton transfer, and the multidimensional mechanism of proton tunneling as determined by the coupling of proton motion to the remaining degrees of freedom in the system. This approach, however, requires diagonalization of the N^2 Hessian matrix for computing the instantaneous normal mode frequencies at each integration time step. In this paper, we introduce an approximation that reduces the computational overhead to the diagonalization of a 2×2 Hessian matrix involving only reaction coordinates. This is accomplished by assuming that the frequencies of the locally harmonic modes are approximately constant along the reaction surface, and that the eigenvalues of the Hessian can be computed to a good approximation by neglecting the off-diagonal Hessian matrix elements that involve both a reaction coordinate and a harmonic mode. The accuracy of this approximate methodology was verified for our system, and is expected to be useful for other systems of biological interest, where proton transfer might be coupled to many other (locally harmonic) degrees of freedom with approximately constant frequencies as a function of the proton displacement.

The paper is organized as follows: The methodology is presented in Sec. II; Sec. II A outlines the calculation of the full-dimensional PES, in terms of an *ab initio* $S1$ reaction surface potential, and Sec. II B describes the semiclassical approach for simulating the photoabsorption spectrum, and the time dependent reactant population. Section III then describes our SC results, and compares them to the results obtained according to more approximate methodologies. The analysis of ESIPT dynamics is concluded in Sec. IV, where the ''mechanism'' suggested by our simulations is compared to the reaction mechanism postulated by recent spectroscopic studies.

II. METHODS

A. Excited state potential energy surface

The excited state intramolecular proton transfer reaction in photoexcited 2-(2′-hydroxyphenyl)–oxazole (HPO) is described in terms of the full-dimensional excited state potential energy surface $V(r_1,r_2,\mathbf{z})$, constructed as a quadratic expansion around a two-dimensional reaction surface potential $V_0(r_1,r_2)$,

$$V(r_1,r_2,\mathbf{z})=V_0(r_1,r_2)+\tfrac{1}{2}[\mathbf{z}-\mathbf{z}_0(r_1,r_2)]\cdot\mathbf{F}(r_1,r_2)\cdot[\mathbf{z}-\mathbf{z}_0(r_1,r_2)], \tag{2.1}$$

where r_1 is the proton displacement, and r_2 is the lowest frequency in-the-plane bending mode ($\sim$170 cm^{-1})—i.e., the hydroxyphenyl–oxazole internal bending mode (see the bending angle $C_1C_2C_7$ in Fig. 1). The other 49 vibrational modes in the system are modeled as locally harmonic degrees of freedom $\mathbf{z}$, with *ab initio* CIS force constants $\mathbf{F}(r_1,r_2)$ and equilibrium positions $\mathbf{z}_0(r_1,r_2)$ parametrized by the reaction coordinates r_1 and r_2. The *ab initio* CIS excited state reaction surface potential $V_0(r_1,r_2)$ is constructed by fully optimizing the geometry of the system with respect to all other degrees of freedom $\mathbf{z}$, subject to the constraint of a fixed value of r_2 for the geometries of the enol, transition state, and keto tautomeric forms. In order to map out the most relevant parts of $V_0(r_1,r_2)$, for the purpose of simulating ESIPT dynamics, *ab initio* energy points are computed holding fixed the r_2 coordinate at five different configurations where the N–O distance is 3.0 Å, 2.8 Å, 2.6 Å, 2.4 Å, and 2.3 Å, respectively (see Fig. 1), since such a range of configurations allows one to compute the energy of all other energetically accessible configurations according to a simple interpolation procedure. In all the *ab initio* calculations the CIS[67] level of quantum chemistry theory—i.e., all single excitations with a spin-restricted Hartree–Fock reference ground state (CIS), using the 6-31G* basis set within the GAUSSIAN 94 series of programs[68]—has been considered for the S_1 state (10 spin-restricted singlet states have been included in the CIS calculation). Since this level of quantum chemistry is expected to give only a good qualitative description of the excited state potential energy surface, we have

explored including electronic correlation in terms of higher levels of quantum chemistry theories, including CIS–MP2, TDDFT, and CASSCF. The CIS/6-31G* level of quantum chemistry was found to be the only current feasible choice for computing both the reaction surface and harmonic frequencies for all energetically accessible configurations: the CIS–MP2 theory was found to have difficulties in the description of potential energy barriers along the proton displacement coordinate (similar difficulties were described in Ref. 33); since TDDFT gradients are yet to be developed, we recalculated the $S1$ surface at the TDDFT level of theory using CIS geometries, but we found that such approximation was not reliable for our system. The computation of the CASSCF(8,8)/6-31G* reaction surface is currently work in progress in our group, and our preliminary results indicate that the CASSCF relative exothermicity, and barrier heights are reproduced by the CIS/6-31G* computations within a 10% error. The current choice of 6-31G* basis set involves approximately 200 basis functions, and corresponds to the limit of our current computational resources in terms of both disk space and available memory for CIS frequencies calculations.

Figure 3 shows the *ab initio* CIS energies for the optimized r_1 geometries at various different r_2 configurations, and the corresponding interpolating curves as a function of r_2. Figure 3 shows that the r_2 coordinate is an efficient tuning mode for proton transfer, since it modulates both the relative distance between the keto and the enol configurations along the r_1 coordinate (see upper panel of Fig. 3), and the potential energy barrier for proton transfer through the transition state (see TS energies in the lower panel of Fig. 3). Figure 3 (see lower panel) also shows that according to our model potential the excited state tautomerization reaction is exothermic.

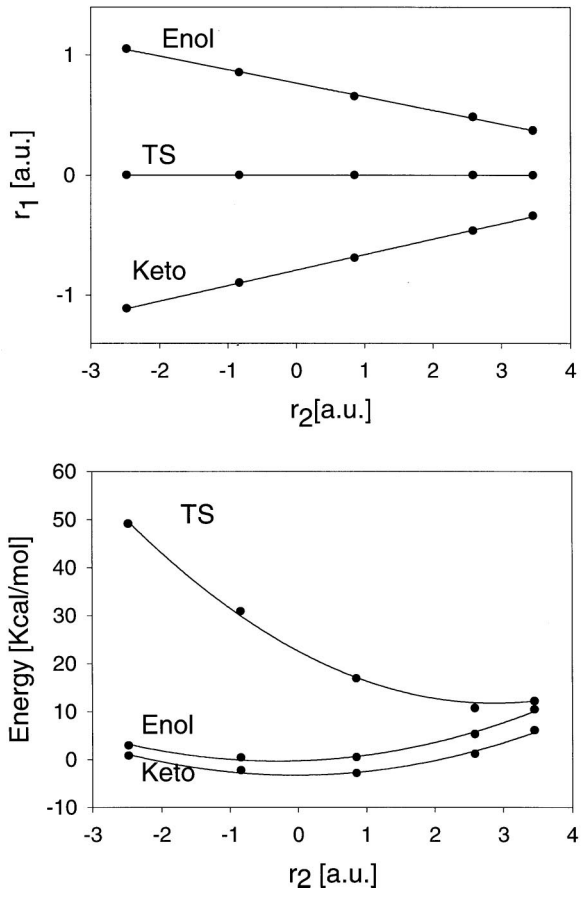

FIG. 3. Proton displacement equilibrium geometries r_1 (upper panel), and CIS/6-31G* *ab initio* energies (lower panel), as a function of the internal oxazole–hydroxyphenyl in-the-plane bending mode r_2.

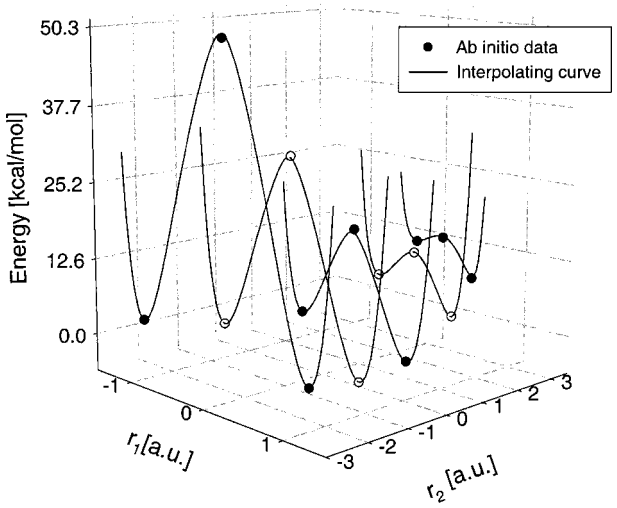

FIG. 4. CIS/6-31G* stationary state energies at various different r_2 configurations, and interpolating curves as a function of the proton displacement r_1. The reaction surface potential $V_0(r_1,r_2)$ is constructed from these interpolating curves, by fitting their adjustable parameters as a function of r_2.

Figure 4 shows the energy profiles at various different r_2 values as a function of r_1. These energy profiles along the r_1 coordinate are constructed in terms of two morse potentials associated with the equilibrium positions of the donor and acceptor configurations, coupled by adjusting the energy barrier to the CIS TS energy for that particular r_2 geometry. The complete reaction surface potential $V_0(r_1,r_2)$ is obtained from these interpolating curves by fitting their adjustable parameters to polynomial expressions of r_2. Figure 4 shows that the proton transfer energy barrier decreases when r_2 increases, i.e., when the distance between the proton donor (hydroxyphenyl) and the proton acceptor (oxazole) decreases.

The equilibrium positions $\mathbf{z}_0(r_1,r_2)$ of the locally harmonic degrees of freedom are computed at an arbitrary point (r_1,r_2), by interpolating between the equilibrium positions at the CIS optimized configurations. The values of $\mathbf{z}_0(r_1,r_2)$ at the optimized configurations are obtained by projecting the geometry difference, with respect to a reference configuration, onto the corresponding normal mode eigenvectors. The equilibrium positions of the 16 out-of-the-plane vibrational modes are found to be independent of the reaction coordinates r_1 and r_2. Therefore, according to the *ab initio* CIS model potential implemented in our calculations, only the 34 in-the-plane vibrational modes are significantly coupled to the proton displacement, including 33 locally harmonic modes $\mathbf{z}$, and the reaction coordinate r_2. Table I describes the complete set of locally harmonic modes $z^{(j)}$ (with $j=1-33$) that influence the ESIPT dynamics according to

TABLE I. Description of the 33 harmonic normal modes **z**, in terms of the stretching (stretch.), bending (bend.), and torsion frequencies and their corresponding reduced masses in parentheses. Frequencies are expressed in cm^{-1} and reduced mass in amu.

Mode description	Frequency in cm^{-1} (reduced mass in amu)
Internal bend.	411.5(7.4), 549.6(5.0)
Hydroxyphenyl and oxazole ring torsion	584.5(7.0), 676.2(6.5), 879.5(7.1), 913.(7.0) 336.4(8.1), 1003.6(7.8), 1077.0(4.8), 1100.6(2.9)
CCH bend., Aromatic C═C stretch., COH bend.	1190.2(1.6), 1202.6(2.1), 1254.8(1.7) 1594.7(1.8), 1682.6(2.9), 1527.4(1.9) 1326.8(1.7), 1550.6(2.2)
Aromatic C–N and C–C stretch., C–O oxazole stretch.	1234.8(2.8), 1282.1(1.5), 1364.5(6.6), 1399.9(2.2)
Alcohol C–O stretch.	1451.7(3.8)
Aromatic C═C stretch.	1605.5(3.1), 1648.4(4.2), 1689.8(4.1) 1763.9(5.3)
C–H stretch.	3370.8(1.1), 3385.1(1.1), 3399.7(1.1) 3415.3(1.1), 3452.4(1.1), 3495.3(1.1)

the model potential introduced by Eq. (2.1). The frequencies $\omega_0^{(j)}$ and reduced masses $\mu^{(j)}$, tabulated in the second column of Table I, are assumed to be independent of the reaction coordinates.

B. Semiclassical approach

The ESIPT dynamics involved in the tautomerization reaction of HPO is analyzed in terms of both the total photoabsorption cross section $\sigma(\lambda)$ of the HPO molecule, as a function of the photolysis wave length λ, and the time-dependent reactant population $P(t)$.

The total photoabsorption cross section $\sigma(\lambda)$ is given by the Fourier transform of the survival amplitude $\xi(t)$,

$$\sigma(\lambda)=\frac{1}{2\pi\hbar}\int_{-\infty}^{\infty}dt\,\xi(t)e^{i\omega t}, \tag{2.2}$$

with $\omega=2\pi c/\lambda$, and

$$\xi(t)\equiv\langle\Psi_0|e^{-i\hat{H}t/\hbar}|\Psi_0\rangle=\langle\Psi_0|\Psi_t\rangle. \tag{2.3}$$

Substituting the time evolution operator in Eq. (2.3) by its coherent state IVR (*vide infra*),[43]

$$e^{-i\hat{H}t/\hbar}=(2\pi\hbar)^{-N}\int d\mathbf{p}_0\int d\mathbf{q}_0\,e^{iS_t(\mathbf{p}_0,\mathbf{q}_0)/\hbar}\times C_t(\mathbf{p}_0,\mathbf{q}_0)|g_{\mathbf{q}_t,\mathbf{q}_t}\rangle\langle g_{\mathbf{q}_0,\mathbf{p}_0}|, \tag{2.4}$$

we obtain the SC–IVR of the survival amplitude,

$$\xi(t)=(2\pi\hbar)^{-N}\int d\mathbf{p}_0\int d\mathbf{q}_0\,C_t(\mathbf{p}_0,\mathbf{q}_0)\times e^{iS_t(\mathbf{p}_0,\mathbf{q}_0)/\hbar}\langle\Psi_0|\mathbf{p}_t,\mathbf{q}_t\rangle\langle\mathbf{p}_0,\mathbf{q}_0|\Psi_0\rangle, \tag{2.5}$$

where the integration variables $(\mathbf{p}_0,\mathbf{q}_0)$ are the initial conditions for classical trajectories, and $\mathbf{q}_t\equiv\mathbf{q}_t(\mathbf{p}_0,\mathbf{q}_0)$ and $\mathbf{p}_t\equiv\mathbf{p}_t(\mathbf{p}_0,\mathbf{q}_0)$ are the time-evolved coordinates and momenta. $\mathbf{q}\equiv(r_1,r_2,\mathbf{z})$ represents the nuclear coordinates collectively, and $\mathbf{p}$ represents their corresponding momenta.

$S_t(\mathbf{p}_0,\mathbf{q}_0)$ is the classical action along this trajectory, obtained by integrating the following equation:

$$\dot{S}_t=\mathbf{p}_t\cdot\dot{\mathbf{q}}_t-H(\mathbf{p}_t,\mathbf{q}_t), \tag{2.6}$$

along with the usual classical equations of motion,

$$\frac{dq(j)}{dt}=\frac{\partial H(\mathbf{q},\mathbf{P})}{\partial p(j)}\quad\text{and}\quad\frac{dp(j)}{dt}=-\frac{\partial H(\mathbf{q},\mathbf{p})}{\partial q(j)}. \tag{2.7}$$

The initial state $|\Psi_0\rangle$, is assumed to be the ground vibrational state of S_0 (Condon approximation),

$$\langle\mathbf{q}|\Psi_0\rangle=\prod_{j=1}^{N}\left(\frac{\alpha_j}{\pi}\right)^{1/4}\exp\left(-\frac{\alpha_j}{2}q(j)^2\right), \tag{2.8}$$

where $N=35$ is the number of coupled degrees of freedom, $q(j)$ is the jth coordinate, and $\alpha_j=\sqrt{k_j\mu^{(j)}/\hbar^2}$, where k_j is the jth harmonic constant, and $\mu^{(j)}$ represents the jth reduced mass.

As presented above, the computational task to compute the survival amplitude $\xi(t)$ is to evaluate the 70-dimensional integral over initial conditions, introduced by Eq. (2.5). This integral is computed according to an importance sampling Monte Carlo technique, where the sampling function of initial conditions $(\mathbf{p}_0,\mathbf{q}_0)$ is defined according to the norm of the coherent state transform of the initial state, $|\langle g_{\mathbf{q}_0,\mathbf{p}_0}|\Psi_0\rangle|$. The wave function for the coherent state $|g_{\mathbf{q}_0,\mathbf{p}_0}\rangle$, introduced by Eq. (2.4), is

$$\langle\mathbf{q}|g_{\mathbf{q}_0,\mathbf{p}_0}\rangle=\prod_{j=1}^{N}\left(\frac{2\gamma^{(j)}}{\pi}\right)^{1/4}\exp\left(-\gamma^{(j)}[q(j)-q_0(j)]^2+\frac{i}{\hbar}p_0(j)[q(j)-q_0(j)]\right), \tag{2.9}$$

and similarly for the wave function $\langle\mathbf{q}|g_{\mathbf{q}_t,\mathbf{p}_t}\rangle$.

The pre-exponential factor $C_t(\mathbf{p}_0,\mathbf{q}_0)$, in Eq. (2.4), involves the monodromy matrix elements that we propagate

according to the adiabatic approximation introduced in Ref. 52. $C_t(\mathbf{p}_0,\mathbf{q}_0)$, introduced by Eq. (2.4), is given by the approximate expression

$$C_t(\mathbf{p}_0,\mathbf{q}_0)=\left[\prod_{j=1}^{N}\tilde{M}_t(j,j)\right]^{1/2}, \tag{2.10}$$

where $\tilde{M}_t(j,j)$ is defined as

$$\tilde{M}_t(j,j)=\frac{1}{2}\left(\tilde{Q}_t(j,j)+i\frac{\tilde{P}_t(j,j)}{\hbar 2\gamma^{(j)}}\right), \tag{2.11}$$

where $\gamma^{(j)}$ are the parameters in the coherent states of Eq. (2.9). The canonical variables $\tilde{Q}_t(j,j)$ and $\tilde{P}_t(j,j)$ are obtained by numerical integration of the following equations of motion:

$$\begin{aligned}&\mu^{(j)}\dot{\tilde{Q}}_t(j,j)=\tilde{P}_t(j,j),\\&\dot{\tilde{P}}_t(j,j)=-\mu^{(j)}[\omega_t^{(j)}]^2\tilde{Q}_t(j,j),\end{aligned} \tag{2.12}$$

with initial conditions $\tilde{Q}_0(j,j)=1$ and $\tilde{P}_0(j,j)=-i\hbar 2\gamma^{(j)}$. The instantaneous normal mode frequencies $\omega_t^{(j)}$, introduced by Eq. (2.12), are obtained by diagonalization of the Hessian $\mathbf{K}_t$ along the classical trajectories.

In order to reduce the computational effort involved in the calculation of the instantaneous normal mode frequencies, we introduce two approximations: First, we assume that the eigenvalues of the Hessian can be obtained to a good approximation by neglecting the off-diagonal matrix elements that involve both a reaction coordinate and a harmonic mode, and second we assume that the frequencies of the locally harmonic modes are approximately constant along the reaction surface (we have observed that these frequencies typically change only up to 20% along the reaction surface). By introducing these two approximation, we therefore reduce the computational effort necessary to obtain the instantaneous eigenfrequencies $\omega_t^{(j)}$ to the diagonalization of a 2×2 Hessian matrix involving only reaction coordinates.

The computational task involved in the propagation of the canonical variables $\tilde{Q}_t(j)$ and $\tilde{P}_t(j)$, associated with the locally harmonic modes $z(j)$ with $j=1-(N-2)$, is reduced by choosing the parameters in the coherent states to be $2\gamma^{(j)}=\omega^{(j)}\mu^{(j)}$. The $(N-2)$ independent equations of motion associated with the locally harmonic modes can then be integrated analytically to obtain

$$\begin{aligned}&\tilde{Q}_t(j,j)=e^{-i\omega^{(j)}t},\\&\tilde{P}_t(j,j)=-i\mu^{(j)}\omega^{(j)}e^{-i\omega^{(j)}t},\end{aligned} \tag{2.13}$$

since these modes are orthogonal among themselves and their frequencies are assumed to be constant along the reaction surface.

Summarizing, $C_t(\mathbf{p}_0,\mathbf{q}_0)$ is computed according to the approximate expression

$$C_t(\mathbf{p}_0,\mathbf{q}_0)=[\tilde{M}_t(1,1)\tilde{M}_t(2,2)]^{1/2}e^{-i\Omega t}, \tag{2.14}$$

where

$$\Omega=\frac{1}{2}\sum_{j=3}^{N}\omega^{(j)}. \tag{2.15}$$

$\tilde{M}_t(1,1)$ and $\tilde{M}_t(2,2)$, in Eq. (2.14), are obtained according to Eq. (2.11), with $\tilde{Q}_t(j,j)$ and $\tilde{P}_t(j,j)$ integrated according to Eqs. (2.12), using the instantaneous normal mode frequencies $\omega_t^{(1)}$ and $\omega_t^{(2)}$ that are obtained through diagonalization of the 2×2 Hessian matrix involving only coordinates r_1 and r_2.

$P(t)$ is defined as the probability that at time t the system is still on the reactant side of the dividing surface (in coordinate space) that separates reactants (enol tautomeric form) and products (keto tautomeric form),

$$P(t)\equiv\langle\Psi_0|e^{i\hat{H}t/\hbar}h(\mathbf{q})e^{-i\hat{H}t/\hbar}|\Psi_0\rangle, \tag{2.16}$$

where $\hat{H}$ is the Hamiltonian operator, and $h(\mathbf{q})$ is a function of the transfering proton coordinate r_1 that is 1(0) on the reactant (product) side of the dividing surface. The SC–IVR of the time dependent reactant population $P(t)$ is obtained by substituting the time evolution operators in Eq. (2.16) by the coherent state IVR, given by Eq. (2.4),

$$\begin{aligned}P(t)=(2\pi\hbar)^{-2N}&\int d\mathbf{p}_0\int d\mathbf{q}_0\int d\mathbf{p}_0'\int d\mathbf{p}_0'\\&\times e^{i(S_t(\mathbf{p}_0,\mathbf{q}_0)-S_t(\mathbf{p}_0',\mathbf{q}_0'))/\hbar}C_t(\mathbf{p}_0,\mathbf{q}_0)C_t^*(\mathbf{p}_0',\mathbf{q}_0')\\&\times\langle\Psi_0|\mathbf{p}_0',\mathbf{q}_0'\rangle\langle\mathbf{p}_t',\mathbf{q}_t'|h|\mathbf{p}_t,\mathbf{q}_t\rangle\langle\mathbf{p}_0,\mathbf{q}_0|\Psi_0\rangle,\end{aligned} \tag{2.17}$$

Eq. (2.17) is useful to perform a ''direct'' calculation of $P(t)$—i.e., without having to store or calculate any other intermediate quantity.

In principle, the most efficient implementation of Eq. (2.17) is the one that samples the more important initial conditions $(\mathbf{p}_0,\mathbf{q}_0)$ and $(\mathbf{p}_0',\mathbf{q}_0')$ for pairs of trajectories that propagate forward in time, and contribute to $P(t)$ at each time t according to the integrand of Eq. (2.17). In practice, however, we found that such approach converges extremely slowly for systems with many degrees of freedom, even when implemented according to a stratified adaptive Monte Carlo technique. We were therefore forced to change the integration variables $(\mathbf{p}_0',\mathbf{q}_0')$ to $(\mathbf{p}_t',\mathbf{q}_t')$, and to optimize convergence for each specific time t by sampling the phase space points $(\mathbf{p}_t',\mathbf{q}_t')$ according to a defensive importance sampling technique.[69]

Equation (2.17) can be written in terms of the new integration variables $(\mathbf{p}_0,\mathbf{q}_0)$ and $(\mathbf{p}_t',\mathbf{q}_t')$, according to

$$\begin{aligned}P(t)=(2\pi\hbar)^{-2N}&\int d\mathbf{p}_0\int d\mathbf{q}_0\int d\mathbf{p}_t'\int d\mathbf{p}_t'\\&\times e^{i(S_t(\mathbf{p}_0,\mathbf{q}_0)-S_t(\mathbf{p}_0',\mathbf{q}_0'))/\hbar}C_t(\mathbf{p}_0,\mathbf{q}_0)C_t^*(\mathbf{p}_0',\mathbf{q}_0')\\&\times\langle\Psi_0|\mathbf{p}_0',\mathbf{q}_0'\rangle I(\mathbf{p}_0,\mathbf{q}_0,\mathbf{p}_t',\mathbf{q}_t')\langle\mathbf{p}_t',\mathbf{q}_t'|\mathbf{p}_t,\mathbf{q}_t\rangle\\&\times\langle\mathbf{p}_0,\mathbf{q}_0|\Psi_0\rangle,\end{aligned} \tag{2.18}$$

where $I(\mathbf{p}_0,\mathbf{q}_0,\mathbf{p}_t',\mathbf{q}_t')$, in Eq. (2.18), is the complex error function

$$\begin{aligned}&I(p_1(t),q_1(t),p_1'(t),q_1'(t);\gamma^{(1)})\\&\quad=\int_{-\infty}^{0}dr\,e^{-\gamma^{(1)}[r-(r_1(t)+r_1'(t))/2-(i/2\gamma^{(1)})(p_1(t)-p_1'(t))]^2},\end{aligned} \tag{2.19}$$

since according to the construction of the reaction surface, presented in Sec. II A, the dividing surface that separates reactants and products is defined as $r_1=0$.

In order to evaluate Eq. (2.18), trajectories are initialized through MC sampling of coordinates and momenta $(\mathbf{p}_0,\mathbf{q}_0)$ according to the localized phase space distribution $|\langle \mathbf{p}_0,\mathbf{q}_0|\Psi_0\rangle|^2$. The partial contribution of a single trajectory to $P(t)$ requires forward propagation from the initial phase point $(\mathbf{p}_0,\mathbf{q}_0)$ to the resulting phase point $(\mathbf{p}_t,\mathbf{q}_t)$ at time t. At this time the trajectory undergoes a coordinate and momentum stochastic hop, $(\mathbf{p}_t,\mathbf{q}_t)\rightarrow(\mathbf{p}_t',\mathbf{q}_t')$, and then evolves backward from $(\mathbf{p}_t',\mathbf{q}_t')$ to the resulting phase point $(\mathbf{p}_0',\mathbf{q}_0')$ at time 0.

The sampling function f_t for coordinates and momenta $(\mathbf{p}_t',\mathbf{q}_t')$ is defined in terms of the overlap of the coherent states at time t as

$$f_t(\mathbf{p}_t',\mathbf{q}_t')=(1-\beta)\Pi_{j=1}^{N}\sqrt{\frac{\delta}{\pi}} \times e^{-\delta[(p_t'(j)-p_t(j))^2+(q_t'(j)-q_t(j))^2]} + \beta\Pi_{j=1}^{N}|\langle p_t'(j),q_t'(j)|p_t(j),q_t(j)\rangle|, \qquad (2.20)$$

where δ is a constant parameter, and the convergence rate β is adjusted according to the dimensionality of the problem. The role of the first term, in Eq. (2.20), is to provide a localized distribution that samples coordinates and momenta $(\mathbf{p}_t',\mathbf{q}_t')$ sufficiently close to $(\mathbf{p}_t,\mathbf{q}_t)$ as to have partial cancellation of the phase in the integrand, while the second term is a broad distribution that is essential to provide an upper bound to the variance when the first term is much smaller than the value of the integrand.

III. RESULTS

Results are presented in two sections. First, Sec. III A presents results for the survival amplitude $\xi(t)$, the photoabsorption spectrum $\sigma(\lambda)$, and the time dependent reactant (enol) population $P(t)$ decay, obtained according to the SC–IVR methodology described in Sec. II B, using the full-dimensional PES described in Sec. II A. Section III A also compares our SC–IVR calculations with the corresponding results obtained according to more approximate semiclassical methodologies, as well as the analysis of the isotopic substitution effect on $P(t)$. Finally, Sec. III B verifies the accuracy and reliability of our methodology by comparing the semiclassical results for $P(t)$, $\sigma(\lambda)$, and $\xi(t)$ with exact full quantum mechanical calculations for a simplified model PES in reduced dimensionality.

Semiclassical trajectories are integrated according to a standard fourth-order Runge–Kutta algorithm,[70] with a 0.024 fs integration step, using the parallel programming model described in Ref. 71. The rather small integration step is necessary to have both energy conservation, and a Jacobian factor $J=\partial(\mathbf{p}_t,\mathbf{q}_t)/\partial(\mathbf{p}_0,\mathbf{q}_0)$ approximately equal to unity throughout the whole simulation. All forces and second derivatives necessary for integrating the equations of motion were calculated using finite difference expressions.

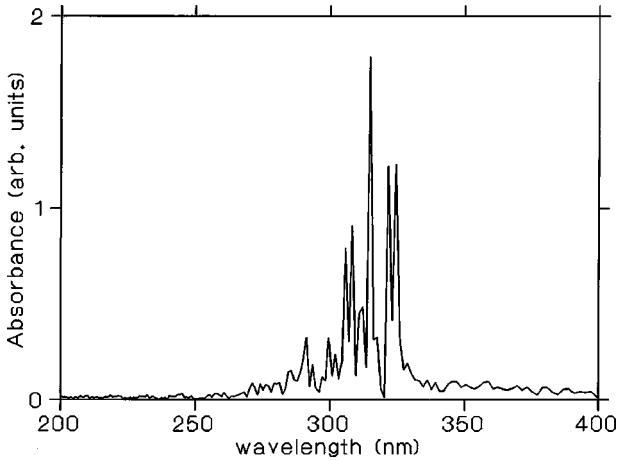

FIG. 5. Semiclassical photoabsorption spectrum of HPO obtained according to the methodology described in Sec. II B, implemented on the full-dimensional S1 PES described in Sec. II A.

A. Full-dimensional model

Figure 5 shows the semiclassical photoabsorption spectrum $\sigma(\lambda)$ of HPO in the gas phase, as a function of the photon wavelength λ. The spectrum was obtained, as described in Sec. II B, propagating 10^6 semiclassical trajectories on the full-dimensional $S1$ PES described in Sec. II A for 200 fs after photoexcitation of the system. Figure 5 shows that some of the overall features of this spectrum resemble those of the experimental absorption spectrum of HPMO in *n*-hexane at room temperature, presented in Fig. 2, including the frequency range (300–330 nm) of the absorption band, and the presence of a superimposed structure with a spacing between peaks of ~11 nm. The assignment of the superimposed structure predicted by our calculations, however, differs from the assignment given by experimental studies of HPMO.[33] According to our calculations, this is a vibronic structure associated with transient excitations of high frequency modes that include internal bending, and ring torsion (see Table I). This assignment is described later in this section in terms of the recurrence features observed in

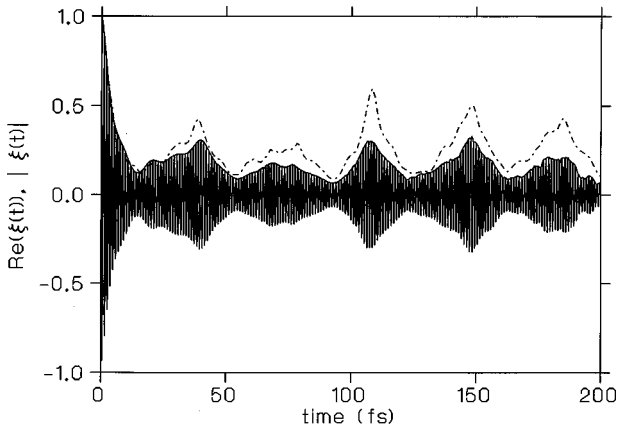

FIG. 6. Real part, and modulus of the survival amplitude $\xi(t)$, obtained according to the semiclassical methodology presented in Sec. II B (solid line), implemented on the full-dimensional S1 PES described in Sec. II A, and the comparison with more approximate semiclassical results for $|\xi(t)|$ obtained according to the classical Wigner model (dashes).

the survival amplitude. In contrast to this interpretation, experimental studies of HPMO have assigned the two peaks at 309 and 322 nm to the vertical excitation, and the 0–0 transition, respectively.

Figure 6 shows the semiclassical results for the real part, and modulus of the survival amplitude $\xi(t)$, for the first 200 fs of dynamics after photoexcitation of the system. This figure shows that there is an ultrafast fall-off of the overlap between the initial and final wave functions (within the first 20 fs of dynamics that is caused by Ψ_t moving away from Ψ_0 as the high frequency modes, associated with hydroxyphenyl and oxazole ring torsion degrees of freedom, move in phase space away from their initial Frank–Condon configurations. This ultrafast relaxation at very short time is responsible for the width of the absorption spectrum in the frequency domain, shown in Fig. 5, and all the subsequent dynamics at longer times determines the superimposed structure but does not affect the position or overall width of the absorption band. The longer time dynamics gives rise to partial recurrences, the most prominent of which occur by 40 fs after photoexcitation of the system. This recurrence feature results from the partial overlap of the initial and final wave functions, caused by the return of the coordinates of high frequency modes to the region of configurational space associated with their initial conditions. This recurrence event is only partial, since at this later time the system is found to be displaced relative to the initial conditions associated with the low frequency modes, e.g., the hydroxyphenyl–oxazole internal bending. The lack of a similar recurrence feature by 80 fs shows the transient character of this vibrational excitation, and indicates that there is significant vibrational energy redistribution even at this very early relaxation time. The spectroscopic consequence of transient vibrations can be observed in Fig. 5 in terms of a rather diffuse vibronic structure with only a few prominent peaks. Figure 6 also compares the modulus of the survival amplitude with the corresponding results obtained according to the classical Wigner model,

$$|\xi(t)| = (2\pi\hbar)^{-2N} \left| \int d\mathbf{q}_0 \int d\mathbf{p}_0 \, F^W(\mathbf{q}_0,\mathbf{p}_0) F^W(\mathbf{q}_t,\mathbf{p}_t) \right|, \tag{3.1}$$

where the Wigner distribution of initial conditions is

$$F^W(\mathbf{p}_0,\mathbf{q}_0) = \int_{-\infty}^{\infty} d\Delta\mathbf{q} \, e^{ip_0\Delta\mathbf{q}/\hbar} \Psi_0^*(\mathbf{q}_0+\Delta\mathbf{q}/2,\mathbf{q}_0)\Psi_0^* \times(\mathbf{q}_0-\Delta\mathbf{q}/2,\mathbf{q}_0), \tag{3.2}$$

and similarly for $F^W(\mathbf{q}_t,\mathbf{p}_t)$. Figure 6 shows that the classical Wigner model is able to describe the early time relaxation, for the first 15 fs of dynamics, and to capture the right timing for recurrences at longer times. However, the classical model is not able to describe the amplitudes associated with these recurrent events as predicted by the more rigorous SC–IVR methodology. Figure 6 thus shows that there is a significant part of the overall relaxation process that is purely classical in nature, including the early time fall off, and the timing for recurrencies, but the magnitude of the recurrencies at longer times is largely controlled by quantum mechanical effects, e.g., tunneling and interference, that are crucial for a proper description of the overall relaxation dynamics in this large polyatomic system.

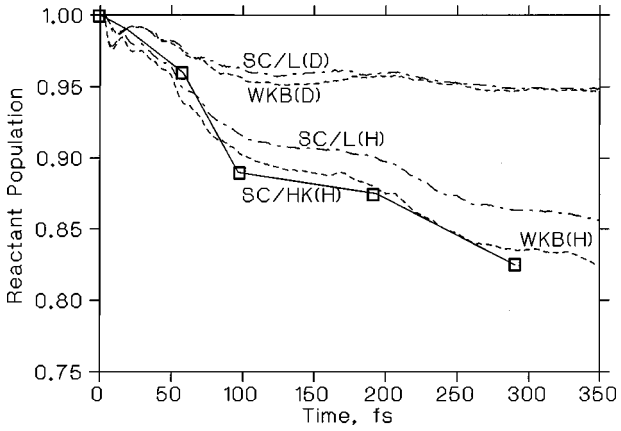

FIG. 7. Time dependent reactant (enol) population decay $P(t)$ (boxes) obtained by simulating the tautomerization dynamics according to the SC methodology presented in Sec. II B, using the full-dimensional PES described in Sec. II A. $P(t)$ is compared to the corresponding results obtained according to the classical Wigner model for the undeuterated [SC/L(H)], and deuterated [SC/L(D)] system, as well as to the corresponding semiclassical results obtained according to the WKB approximation for the undeuterated [WKB(H)], and deuterated [WKB(D)] system.

Figure 7 shows the time dependent reactant (enol) population $P(t)$ for the first 300 fs of dynamics after photoexcitation of the system, as predicted by the SC–IVR methodology implemented on the full-dimensional PES. Figure 7 shows that the reactant population decays about 17% during the first 300 fs, according to a relaxation process that cannot be described by a single exponential function. The reason for this is that the tautomerization reaction involves proton transfer through an effective potential energy barrier that is strongly modulated by both ultrafast vibrational energy redistribution among high frequency modes and the motion along the internal hydroxyphenyl–oxazole bending coordinate. We have calculated $P(t)$ at only five different times, within the first 300 fs, since calculating $P(t)$ at each time requires a separate calculation of a 140-dimensional integral and demands running approximately 10^7 semiclassical trajectories. This enormous computational effort aims to produce the most rigorous simulations to date of the excited state time dependent proton-transfer dynamics, associated with the tautomerization reaction of a relatively large polyatomic system, and demonstrates for the first time that is possible to converge the full double phase space SC–IVR of $P(t)$ for a system with 35 coupled degrees of freedom even after 300 fs of dynamics. Furthermore, these rigorous results allow us to estimate the importance of quantum mechanical effects on the relaxation dynamics of a large polyatomic system, and to evaluate the reliability of more approximate calculations based on the WKB approximation,[36] or the Wigner classical model,[72]

$$P(t) = (2\pi\hbar)^{-2N} \int d\mathbf{q}_0 \int d\mathbf{p}_0 \, F^W(\mathbf{q}_0,\mathbf{p}_0) h(\mathbf{q}_t), \tag{3.3}$$

where $F^W(\mathbf{q}_0,\mathbf{p}_0)$ is the Wigner distribution of initial conditions introduced by Eq. (3.2), and $h(\mathbf{q}_t)$ is the function of the transfering proton introduced by Eq. (2.16).

Figure 7 compares the reactant population $P(t)$ given by the SC–IVR methodology, implemented for the undeuterated system SC/HK(H), and the corresponding results obtained according to the classical Wigner model SC/L(H), and the WKB approximation WKB(H). The first feature to note is that the classical Wigner model provides a good description for proton transfer within the first 20 fs of dynamics, during which the first encounter between the proton donor and the proton acceptor functional groups takes place, and also describes quite accurately the time at which proton transfer is favorable at longer times, since this is primarily determined by the reorganization of classical degrees of freedom. Figure 7 shows that a significant amount ($\sim$75%) of the total reactant population decay is well predicted by the classical Wigner model, with only $\sim$25% of the reactant population due to quantum mechanical effects such as tunneling and interference. This extra probability of proton transfer is fairly well reproduced by the stochastic semiclassical method based on the WKB approximation. These results are therefore totally consistent with the comparison of results for $\xi(t)$ presented in Fig. 6.

Figure 7 also compares $P(t)$ for the undeuterated system with the reactant population decay for the deuterated system, as predicted by the WKB approximation, and the classical Wigner model. Both methods predict that the reactant population decay is significantly affected by isotopic substitution. The agreement between these two calculations also shows that the reactant population decay for deuterated systems is almost completely classical, since the zero point energy is lower and therefore the probability of proton tunneling is much smaller.

Having validated the reactant population decay predicted by the WKB approximation, Fig. 8 shows $P(t)$ for the undeuterated system for the first 18 ps of dynamics after photoexcitation of the system (solid line). Figure 8 also includes the raw data convoluted with a typical instrument resolution function (FWHM=150 fs) which would be appropriate to make comparisons with ultrafast spectroscopic signals, analogous to those presented in Fig. 2 for HPMO in 3-methylpentane. Figure 8 also shows, once again, that the reactant population decay cannot be described by a single exponential function.

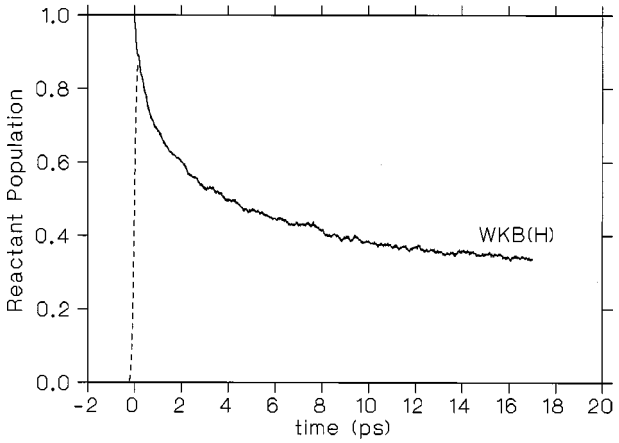

FIG. 8. Time dependent reactant (enol) population decay obtained by simulating the first 18 ps of tautomerization dynamics according to the semiclassical stochastic method based on the WKB approximation.

B. Simplified model

In this section we compare the semiclassical results of simulations on a simplified three-dimensional excited state PES to the corresponding full quantum mechanical calculations for the early time relaxation dynamics of photoexcited HPO. The comparison presented in this section for the wave packet motion, reactant population decay, the survival amplitude, and the photoabsorption spectrum, aims to check the accuracy and reliability of the semiclassical methodology as implemented for the full-dimensional model potential in Sec. III A. This comparison, together with similar tests reported before,[52] provide important documentation on the ability of these new semiclassical techniques to simulate realistic excited state proton transfer reactions, where proton motion is found to be significantly coupled to the motion of the remaining degrees of freedom in the system.

The PES V given by Eq. (2.1) can be written for the reduced three-dimensional space as

$$V(r_1,r_2,R)\approx V_0(r_1,r_2)+\tfrac{1}{2}[\omega_R(r_1,r_2)]^2 \times[R-R_0(r_1,r_2)]^2, \tag{3.4}$$

in terms of a global reorganization coordinate $R\equiv|\mathbf{z}|$—i.e., the norm of the 33-dimensional vector $\mathbf{z}$—that describes on average the motion of the locally harmonic degrees of freedom $\mathbf{z}$ that are significantly coupled to the proton displacement. $R_0(r_1,r_2)$ is the norm of $\mathbf{z}_0(r_1,r_2)$, and the average harmonic frequency $\omega_R(r_1,r_2)$ is computed according to the following expression:

$$\omega_R(r_1,r_2)\equiv\left(\frac{\Sigma_{j=1}^{N}\mu^{(j)}*[\omega^{(j)}(r_1,r_2)]^2*z_0^{(j)}(r_1,r_2)^2}{R_0(r_1,r_2)^2}\right)^{1/2}, \tag{3.5}$$

where $\mu^{(j)}$, $\omega^{(j)}$, and $z^{(j)}$ correspond to the reduced mass, frequency and displacement of the instantaneous normal mode j.

Figure 9 compares the evolution of the semiclassical wave packet $\rho(\mathbf{r})=\Psi^*(\mathbf{r})\Psi(\mathbf{r})$ in the space of reaction coordinates $\mathbf{r}$—i.e., after integrating out the reorganization coordinate R—to the corresponding full quantum mechanical results at various different times during the early time relaxation. Wave packets are represented by five contour lines equally spaced by 0.03 units in the 0.005–0.155 range of amplitude. The distribution of population into reactant and tautomer configurations can be visualized in Fig. 9 in terms of the probability density that lies on either of the two sides of the dividing surface represented by the transition state at $r_1=0$.

As illustrated by panels (a) and (b), the system is initially localized at the Franck–Condon region with $(r_1,r_2)\approx(-0.3,-1.12)$ a.u., and moves along the r_2 coordinate diminishing the $O^{(8)}$–$N^{(9)}$ distance during the first 75 fs after photoexcitation of the system. Panel (b) shows the wave

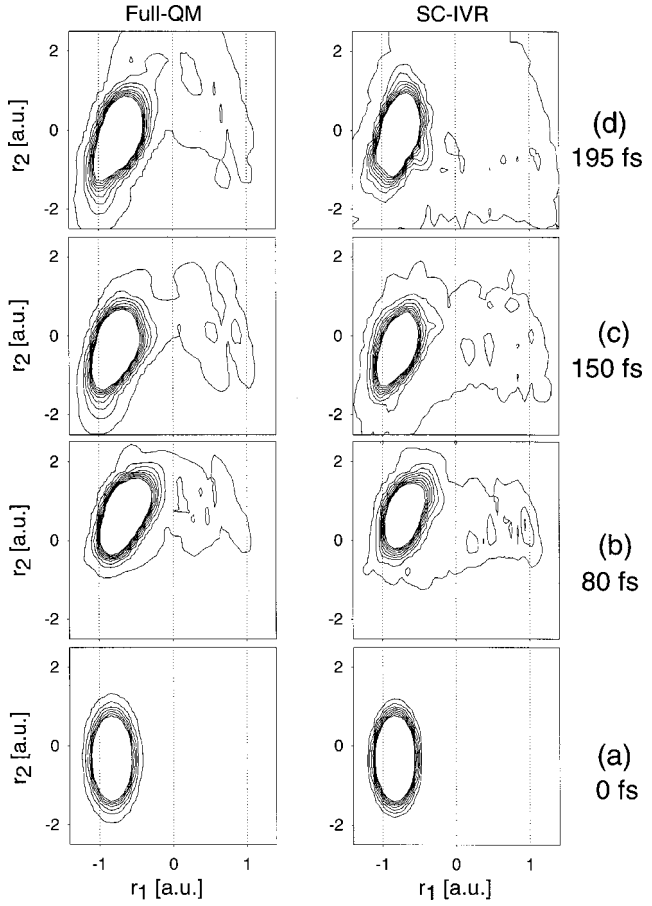

FIG. 9. Comparison of semiclassical and full quantum mechanical wave packets $\rho(\mathbf{r})=\Psi^*(\mathbf{r})\Psi(\mathbf{r})$, reduced to the space of reaction coordinates r_1 and r_2 at various different times during the early time relaxation after photoexcitation of the system [panel (a), 0 fs; panel (b), 80 fs; panel (c), 150 fs; panel (d), 195 fs]. Wave packets are represented by five contour lines equally spaced by 0.045 units in the 0.005–0.185 range of amplitude.

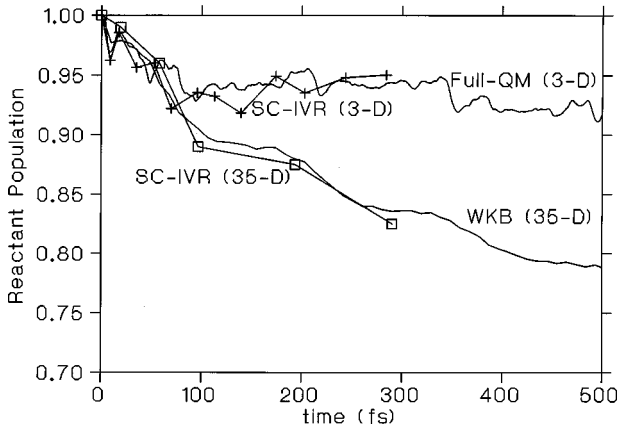

FIG. 10. Comparison between the semiclassical time dependent reactant population $P(t)$ (plus symbols), and the corresponding full quantum mechanical results [solid line, full-QM(3D)] for the early time tautomerization dynamics, as described by the model in reduced dimensionality. These results are also compared to the reactant population decay described by the model in full dimensionality (35D), that includes the proper description of vibrational energy redistribution at longer times.

packet right after reaching a turning point along the internal bending coordinate during the initial relaxation process. At this point the effective barrier heights are minimum and proton transfer is most favorable. The semiclassical results reproduce the exact full quantum evolution of the system and describe correctly the shape and position of the wave packet along the reaction surface potential.

At later times [see panel (c)], the wave packet moves back to the Franck–Condon region within approximately 150 fs, a period that corresponds approximately to the harmonic frequency of the internal bending mode. This panel also shows that the semiclassical results describe properly the amount of products (keto tautomer) formed after the first oscillation period along the $N^{(9)}$–$O^{(8)}$ distance.

At even later times [see panel (d)], the wave packet moves again towards the region of low energy barriers, following the vibrational motion associated with the internal bending mode. The comparison with full quantum mechanical results, in terms of the overall shape and position of the wave packet, shows that the description provided by the approximate SC–IVR method is once again very satisfactory.

Figure 10 compares the SC time dependent reactant population $P(t)$ with the corresponding full quantum mechanical results for the early time tautomerization dynamics, simulated on the three-dimensional model potential introduced by Eq. (3.4). $P(t)$ is obtained according to Eq. (2.17), as described in Sec. II B, projecting the time dependent wave packet into the reactant side of the dividing surface (in coordinate space) that separates both tautomeric forms. This figure also compares the results of $P(t)$ obtained for the model in reduced dimensionality, with the reactant population decay obtained for the 35-dimensional model PES.

The comparison of the SC reactant population decay with the results obtained according to full quantum mechanical calculations shows that all the dynamical features are properly described by the SC approach, including the initial population decay within the first 75 fs of dynamics, and the plateau at longer times with a superimposed modulation. These features can be interpreted in terms of the wave packet motion described earlier in this section. The initial population decay within the first 100 fs, corresponds to the motion along the internal bending coordinate that brings the proton donor (hydroxyphenyl) and proton acceptor (oxazole) functional groups close together, reducing both the proton tunneling barrier heights and the distance along the r_1 coordinate between both tautomeric forms.

The comparison of $P(t)$ from this three-dimensional to that from the full 35-dimensional model shows that the three-dimensional model properly describes the early time relaxation during the first 100 fs. The model potential in reduced dimensionality gives a population decay with a more prominent superimposed structure, since here the reorganization of the remaining degrees of freedom in the system is described by a single global coordinate R with a characteristic time of about 43 fs. The most important difference between the 3D and the 35D models is that the reactant population for the full-dimensional model continues to decrease for times beyond 100 fs (with significant drops at time intervals of ~150 fs after an initial 75 fs decay time), while that for the 3D model remains approximately constant after the initial 100

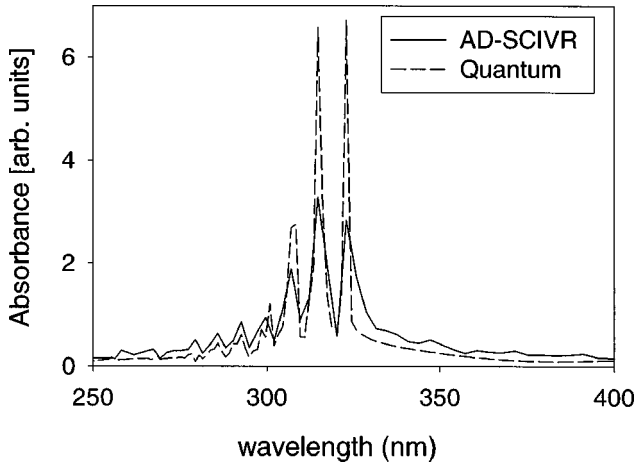

FIG. 11. Semiclassical HPO photoabsorption spectrum (solid line) and the corresponding full quantum mechanical results $\sigma(\lambda)$ (dashed line), as a function of the photon wave length λ.

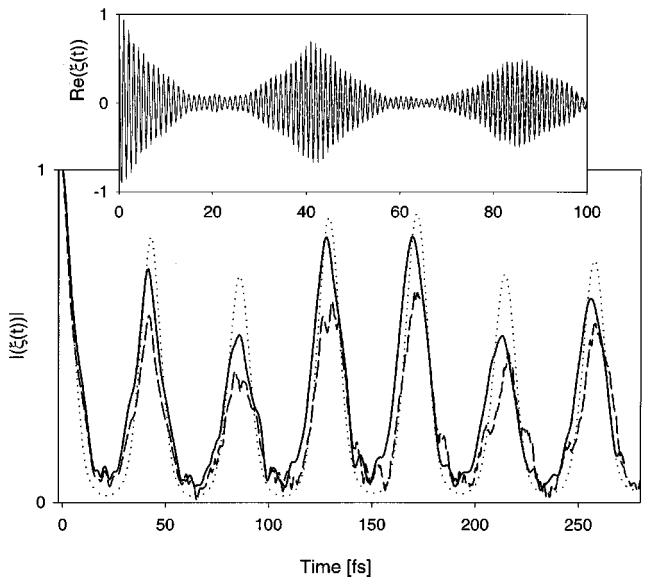

FIG. 12. Upper panel: Comparison of the real part of the survival amplitude $\xi(t)$, obtained according to the SC–IVR (solid line), and full QM calculations (dashes) for the model in reduced dimensionality. Lower panel: comparison of the modulus of the survival amplitude $\xi(t)$, obtained according to the SC–IVR (solid line), the classical Wigner model (dots), and full QM calculations (dashes) for the simplified model in reduced dimensionality.

fs. The reason for this is that the reactant population reaches an equilibrium in the three-dimensional model as a result of recrossing events, since there are no other coupled modes where the internal energy can be redistributed. This natural limitation of the three-dimensional model shows the importance of including explicitly the motion of the remaining degrees of freedom in the system, in order to model of proton transfer as coupled to vibrational energy redistribution at longer times.

Figure 11 shows the comparison of the semiclassical HPO absorption spectrum to the corresponding full quantum mechanical results for the 3D model, as a function of the photon wavelength λ. The vertical transition between the ground electronic state and the $S1$ PES has been rescaled by a factor of 0.74 to correct approximately for the energy shift usually introduced by the *ab initio* CIS calculations. This figure shows that the semiclassical results reproduce the overall qualitative features of the full quantum mechanical spectrum, in terms of the overall shape, as well as the spacing and widths of the superimposed structure of vibronic bands. However, there are small differences in the intensity profile of the semiclassical band when compared to the full quantum mechanical results. The origin of these discrepancies can be traced to small deviations observed in the survival amplitude, as discussed later in this section.

The physics involved in the dynamics of relaxation responsible for the spectroscopic features observed in the photoabsorption spectrum can be addressed in terms of the analysis of the phase space dynamics of semiclassical trajectories. The photolysis event populates excited vibrational states of both the internal bending and the reorganization modes on the excited electronic state PES. The molecule thus vibrates along these modes as it undergoes tautomerization whenever the configuration of the system is favorable for proton transfer to occur. Therefore, the origin of the structure in the photoabsorption spectra is the transient vibration of internal bending and reorganization modes on the reactant side of the dividing surface. In contrast to the spectrum obtained for the model in full dimensionality, the $\nu = 0-6$ vibronic bands are sharp and well defined. In the absence of the other modes involved in ultrafast vibrational energy redistribution, tautomerization is the only possible mechanism that can damp out the oscillatory motion of the reorganization coordinate, and therefore this motion is preserved for much longer time.

Figure 12 shows the comparison of the SC–IVR result for the survival amplitude $\xi(t)$ during the first 250 fs of dynamics after photoexcitation of the system, to the corresponding result obtained from the full quantum mechanical calculation and from the classical Wigner model, all for the 3D model. This figure shows that with the exception of small deviations in the shape of the envelope of the survival amplitude, the semiclassical results are in very good agreement with the full quantum mechanical calculations throughout the whole dynamical range of proton transfer, starting with an ultrafast fall-off of the overlap between the initial and final wave functions (within the first 22 fs of dynamics) that is caused by Ψ_t moving away from Ψ_0 as the reorganization coordinate is displaced relative to its initial position. This ultrafast relaxation at short times is responsible for the broad envelope of the absorption spectrum in the frequency domain seen in Fig. 11, and all the subsequent dynamics at longer times determines the structure in the frequency spectrum but does not affect the position or overall width of the absorption band. The longer time dynamics gives rise to a recurrence feature of the survival amplitude at about 43 fs. The amplitude of this recurrence feature is slightly more pronounced in the full quantum amplitude than in the semiclassical calculations. In this simplified model, the partial overlap of the initial and final wave functions is caused by the displacement of the internal bending mode relative to its initial position when the reorganization coordinate returns to the Franck–Condon region at time t.

IV. SUMMARY AND CONCLUSIONS

We have shown in this paper how the ultrafast ESIPT reaction associated with the keto-enolic tautomerization reaction of photoexcited HPO can be investigated in terms of an approximate semiclassical initial value representation method, and a full-dimensional *ab initio* CIS model PES. These calculations constitute the first effort to give a rigorous interpretation of ESIPT, as coupled to the motion of the remaining degrees of freedom in the system, in terms of a quantitative description of reaction dynamics from first principles.

We have shown how to extend the simplified three-dimensional model developed in our previous study of excited state proton transfer dynamics to incorporate the proper description of vibrational energy redistribution in the model of excited state reaction dynamics. We have shown that this could be accomplished by first calculating the full-dimensional excited state PES, at the CIS level of quantum chemistry, and then solving accurately the dynamical equations for motion on these calculated surfaces.

We have demonstrated the capabilities of the approximate initial value representation method to study ESIPT in photoexcited HPO, showing consistency between the SC–IVR and more approximate semiclassical methods, based on the WKB approximation, and the classical Wigner model. We have also demonstrated the reliability of the semiclassical methodology to model ESIPT in photoexcited HPO, by showing agreement with full quantum mechanical calculations in the description of the wave packet motion, the reactant population decay, the survival amplitude, and the absorption spectrum for a simplified three-dimensional model potential.

The SC method was specifically designed to avoid the computational bottleneck for applications of the SC–IVR to large molecular systems, which is caused by the calculation of the monodromy matrix elements involved in the pre-exponential factor of the semiclassical amplitude. With such an approach we have demonstrated for the first time that it is possible to converge the SC–IVR for both the survival amplitude $\xi(t)$ and the time dependent reactant probability $P(t)$ for a system with 35 coupled degrees of freedom, for the first 300 fs of dynamics after photoexcitation of the system. These semiclassical calculations were useful for estimating the validity of more approximate semiclassical methods, based on the WKB approximation and the classical Wigner model.

We have shown that the reaction mechanism suggested by our calculations differs from the barrierless (or near barrierless) reaction mechanism postulated by recent spectroscopic studies of HPMO, that were based on stabilization of the keto tautomer according to out-of-the-plane twisting motion around the interaromatic C–C bond.[33,34] According to our calculations, proton transfer is not a barrierless process, and it should be possible to observe a significant isotopic effect by probing the time dependent reactant population decay with picosecond (or subpicosecond) resolution. Out-of-the-plane rotations are found to be approximately uncoupled from proton transfer, and rather than stabilizing the system relative to the corresponding planar geometries they produce destabilization to higher energy configurations. Our simulations, however, do not rule out the possibility of detecting keto rotamers when conformational changes are thermally produced.

We have demonstrated that SC calculations predict the HPO absorption spectrum to be similar to the experimental absorption spectrum of HPMO, an asymmetric absorption band in the 300–330 nm frequency range, with a diffuse superimposed structure where the peaks are spaced by ~11 nm. In contrast to experimental studies of HPMO, where the two peaks at 309 and 322 nm were assigned to the vertical excitation and the 0–0 transition, respectively, our calculations show the peaks to correspond to a vibronic structure associated with transient excitations of internal bending and ring torsion modes in the 336–411 cm^{-1} frequency range. We have shown that proton transfer is also significantly coupled to the lowest frequency in-the-plane bending mode ($\sim$177 cm^{-1}), although the SC absorption spectrum does not show a structure associated with the N–O stretching mode. The low frequency mode changes the N–O distance, and therefore modifies both the height and width of the proton transfer energy barrier.

ACKNOWLEDGMENTS

We gratefully acknowledge financial support from the Director, Office of Science, Office of Basic Energy Sciences, Chemical Sciences Division of the U.S. Department of Energy under Contract No. DE-AC03-76SF00098, Lawrence Berkeley National Laboratory, and by the National Science Foundation under Grant No. CHE-97-32758. We also acknowledge a generous allocation of supercomputing time from the National Energy Research Scientific Computing Center (NERSC). V.G. gratefully acknowledges U.A.B and Professor J. M. Lluch and Professor M. Moreno for the doctoral fellowship that concludes with the realization of this work.

[1] Y. Tsuchiya, T. Tamura, M. Fujii, and M. Ito, J. Phys. Chem. **92**, 1760 (1988).
[2] Shin-ichi Nagaoka, Y. Shinde, K. Mukai, and U. Nagashima, J. Phys. Chem. A **101**, 3061 (1997).
[3] S. J. Formosinho and J. Arnaut, J. Photochem. Photobiol., A **75**, 21 (1993).
[4] K. Fuke, H. Yoshiuchi, and K. Kaya, J. Phys. Chem. **88**, 5840 (1984).
[5] A. Engeland, T. Bultmann, N. P. Ernsting, M. A. Rodriguez, and W. Thiel, Chem. Phys. **163**, 42 (1992).
[6] P. Barbara, P. K. Walsh, and L. E. Brus, J. Phys. Chem. **93**, 29 (1989).
[7] G. Yang, F. Morlet-Savary, Z. Peng, S. Wu, and J. Fouassier, Chem. Phys. Lett. **256**, 536 (1996).
[8] L. Premvardhan and L. Peteanu, Chem. Phys. Lett. **296**, 521 (1998).
[9] A. Dohual, F. Amat-Guerri, Acuña, and K. Yoshihara, Chem. Phys. Lett. **217**, 619 (1994).
[10] A. Dohual, F. Amat-Guerri, and Acuña, J. Phys. Chem. **99**, 76 (1995).
[11] M. Brauer, M. Mosquera, J. L. Perez-Lustres, and P. Flor-Rodriguez, J. Phys. Chem. **102**, 10736 (1998).
[12] S. M. Dennison, J. Guharay, and P. K. Sengupta, Spectrochim. Acta, Part A **55**, 1127 (1999).
[13] G. J. Smith and K. R. Markham, J. Photochem. Photobiol., A **118**, 99 (1998).
[14] A. Warshel, *Computer Modeling of Chemical Reactions in Enzymes and Solutions* (Wiley, New York, 1991).
[15] D. S. English, K. Das, K. D. Ashby, J. Park, J. W. Petrich, and E. W. Castner, J. Am. Chem. Soc. **119**, 11585 (1997).

[16] K. Das, D. S. English, and J. W. Petrich, J. Am. Chem. Soc. **119**, 2763 (1997).
[17] P. K. Agarwal, S. P. Webb, and S. Hammes-Schiffer, J. Am. Chem. Soc. **122**, 4803 (2000).
[18] X. Kopfer, Adv. Photochem. **10**, 311 (1977).
[19] D. A. Parthenopoulos, D. McMorrow, and M. Kasha, J. Phys. Chem. **95**, 2668 (1991).
[20] Acuña, F. Amat-Guerri, A. Costela, A. Dohual, J. M. Figuera, F. Florido, and R. Sastre, Chem. Phys. Lett. **98**, 187 (1991).
[21] R. M. Tarkka and S. A. Jenekhe, Chem. Phys. Lett. **260**, 533 (1996).
[22] S. Møller, K. B. Andersen, J. Spanget-Larsen, and J. Waluk, Chem. Phys. Lett. **291**, 51 (1998).
[23] D. Haarrer, Jpn. J. Appl. Phys. **26**, 3362 (1986).
[24] R. C. Haddon and F. H. Stillinger, in *Molecular Electronic Devices*, edited by F. L. Carter (Marcel Dekker, New York, 1987).
[25] H. Sixl and D. Higelin, in *Molecular Electronic Devices*, edited by F. L. Carter (Marcel Dekker, New York, 1987).
[26] S. Takeuchi and T. Tahara, Chem. Phys. Lett. **277**, 340 (1997).
[27] S. Takeuchi and T. Tahara, J. Phys. Chem. **102**, 7740 (1998).
[28] R. Lopez Martens, P. Long, D. Solgadi, B. Soep, J. Syage, and Ph. Millie, Chem. Phys. Lett. **273**, 219 (1997).
[29] M. Chachisvilis, T. Fiebig, A. Douhal, and A. H. Zewail, J. Phys. Chem. **102**, 669 (1998).
[30] K. Tahara, H. Honjo, T. Tanaka, O. Y. Kohauchi, and Y. Endo, J. Chem. Phys. **110**, 1969 (1999).
[31] T. Kar, S. Scheiner, and M. Cuma, J. Chem. Phys. **111**, 849 (1999).
[32] A. Douhal, F. Lahmani, A. Zehnacker-Rention, and F. Amat-Guerri, J. Phys. Chem. **98**, 12198 (1994).
[33] V. Guallar, M. Moreno, J. M. Lluch, F. Amat-Guerri, and A. Douhal, J. Phys. Chem. **100**, 19789 (1996).
[34] A. Dohual, F. Lahmani, A. Zehnacker-Rontien, and F. Amat-Guerri, in *Fast Elementary Processes in Chemical and Biological Systems*. AIP Conference Proceedings No. 346, edited by X. Tramer (American Institute of Physics, New York), p. 383.
[35] A. Douhal, T. Fiebig, M. Chachisuilis, and A. H. Zewail, J. Phys. Chem. **102**, 1657 (1998).
[36] N. Makri and W. H. Miller, J. Chem. Phys. **91**, 4026 (1989).
[37] T. Carrington, Jr. and W. H. Miller, J. Chem. Phys. **84**, 4364 (1986).
[38] S. Hammes-Schiffer and J. C. Tully, J. Chem. Phys. **101**, 4657 (1994).
[39] J. Y. Fang and S. Hammes-Schiffer, J. Chem. Phys. **107**, 8933 (1997).
[40] W. H. Miller, J. Chem. Phys. **62**, 1899 (1975).
[41] V. A. Benderskii, V. I. Goldanskii, and D. E. Makarov, Phys. Rep. **233**, 195 (1993).
[42] F. Grossmann and E. J. Heller, Chem. Phys. Lett. **241**, 45 (1995).
[43] M. F. Herman and E. Kluk, Chem. Phys. **91**, 27 (1984).
[44] K. G. Kay, J. Chem. Phys. **107**, 2313 (1997).
[45] H. Ushiyama and K. Takatsuka, J. Chem. Phys. **106**, 7023 (1997).
[46] B. C. Garrett and D. G. Truhlar, J. Chem. Phys. **79**, 4931 (1983).
[47] A. Warshel and Z. T. Chu, J. Chem. Phys. **93**, 4003 (1990).
[48] J. Cao and G. A. Voth, J. Chem. Phys. **101**, 6168 (1994).
[49] D. Borgis and J. T. Hynes, J. Chem. Phys. **94**, 3619 (1991).
[50] S. Keshavamurthy and W. H. Miller, Chem. Phys. Lett. **218**, 189 (1994).
[51] B. Spath and W. H. Miller, J. Chem. Phys. **104**, 95 (1996).
[52] V. Guallar, V. S. Batista, and W. H. Miller, J. Chem. Phys. **110**, 9922 (1999).
[53] Z. Smedarchina, M. Z. Zgierski, W. Siebrand, and P. M. Kozlowski, J. Chem. Phys. **109**, 1014 (1998), and references therein.
[54] V. A. Benderskii and D. E. Makarov, Chem. Phys. **170**, 275 (1993).
[55] M. Morillo and R. I. Cukier, J. Chem. Phys. **92**, 4833 (1990).
[56] A. Suarez and R. Silbey, J. Chem. Phys. **94**, 4809 (1991).
[57] J. Aqvist and A. Warshel, Chem. Rev. **93**, 2523 (1993).
[58] D. G. Truhlar, Y. P. Liu, G. K. Schenter, and B. C. Garrett, J. Phys. Chem. **98**, 8396 (1994).
[59] D. Borgis, G. Tarjus, and H. Azzuoz, J. Phys. Chem. **96**, 3188 (1992).
[60] D. Borgis, G. Tarjus, and H. Azzuoz, J. Phys. Chem. **97**, 1390 (1992).
[61] D. Laria, G. Ciccoti, M. Ferrario, and R. Kapral, J. Chem. Phys. **97**, 378 (1992).
[62] A. Fedorowicz, J. Mavri, P. Bala, and A. Koll, Chem. Phys. Lett. **289**, 457 (1998).
[63] M. T. M. Koper and G. A. Voth, Chem. Phys. Lett. **282**, 100 (1998).
[64] Y. G. Boroda, A. Calhoun, and G. A. Voth, J. Chem. Phys. **107**, 8940 (1997).
[65] Y. Guo, A. K. Wilson, C. F. Chabalowski, and D. L. Thompson, J. Chem. Phys. **109**, 9258 (1998).
[66] Y. Guo, S. Li, and D. L. Thompson, J. Chem. Phys. **107**, 2853 (1997).
[67] J. A. Pople, J. B. Foresman, M. Head-Gordon, and M. J. Frisch, J. Phys. Chem. **96**, 135 (1992).
[68] M. J. Frisch, G. W. Trucks, H. B. Schlegel *et al.*, GAUSSIAN 94 (Gaussian Inc., Pittsburgh, PA 1995).
[69] T. C. Hesterberg, Technometrics **37**, 185 (1995).
[70] W. H. Press, B. P. Flannery, S. A. Teukolsky, and W. T. Vetterling, *Numerical Recipes* (Cambridge University Press, Cambridge, 1986).
[71] V. S. Batista and W. H. Miller, J. Chem. Phys. **108**, 498 (1998).
[72] E. J. Heller, J. Chem. Phys. **65**, 1289 (1976).